

Intertwined quantum phase transitions in the Zr chain

N. Gavrielov^{1,*}, A. Leviatan^{1,**}, and F. Iachello^{2,***}

¹Racah Institute of Physics, The Hebrew University, Jerusalem 91904, Israel

²Center for Theoretical Physics, Sloane Physics Laboratory, Yale University, New Haven, Connecticut 06520-8120, USA

Abstract. We introduce the notion of intertwined quantum phase transitions (IQPTs), for which a crossing of two configurations coexists with a pronounced shape-evolution of each configuration. A detailed analysis in the framework of the interacting boson model with configuration mixing, provides evidence for this scenario in the Zr isotopes. The latter exhibit a normal configuration which remains spherical along the chain, but exchanges roles with an intruder configuration, which undergoes first a spherical to prolate-deformed [U(5)→SU(3)] QPT and then a crossover to γ -unstable [SU(3)→SO(6)].

Quantum phase transitions (QPTs) are qualitative changes in the properties of a physical system, induced by a variation of parameters that appear in the quantum Hamiltonian. In nuclear physics, most of the attention in the study of QPTs, has been devoted to shape phase transitions in a single configuration, described by a single Hamiltonian, $\hat{H} = (1 - \xi)\hat{H}_1 + \xi\hat{H}_2$, where ξ is the control parameter. As ξ changes from 0 to 1, the eigenvalues of the system change from those of \hat{H}_1 to those of \hat{H}_2 . For sake of clarity, we denote these phase transitions Type I. The latter have been observed in the neutron number 90 region, *e.g.*, for Nd-Sm-Gd isotopes [1].

A different type of phase transitions occurs when two (or more) configurations coexist [2]. In this case, the quantum Hamiltonian has a matrix form with entries: $\hat{H}_A(\xi^A)$, $\hat{H}_B(\xi^B)$, $\hat{W}(\omega)$, where the indices A, B denote the two configurations and \hat{W} denotes their coupling. We call for sake of clarity these phase transitions Type II [3], to distinguish them from those of a single configuration. Type II QPTs have been observed in nuclei near shell closure, *e.g.*, in the light Pb-Hg isotopes [4], albeit with strong mixing between the two configurations. In the present contribution, we explore a situation where in parallel to the crossing, each configuration maintains its purity and its own shape-evolution with nucleon number. We refer to such a scenario as intertwined quantum phase transitions (IQPTs) in the sense that Type I and Type II coexist, and show empirical evidence for it in the Zr chain [5].

The $_{40}\text{Zr}$ isotopes have been recently the subject of several experimental [6–10] and theoretical investigations, including mean-field based methods [11–13] and the Monte-Carlo shell-model (MCSM) [14]. We adapt here the algebraic approach of the Interacting Boson Model (IBM) [15], with bosons representing valence nucleon pairs counted from the nearest closed shells. This provides

a simple tractable framework, where phases of quadrupole shapes: spherical, prolate-deformed and γ -unstable correspond to U(5), SU(3) and SO(6) dynamical symmetries.

To be specific, we use the configuration mixing model (IBM-CM) of [16], and write the Hamiltonian not in matrix form, but rather in the equivalent form

$$\hat{H} = \hat{H}_A^{(N)} + \hat{H}_B^{(N+2)} + \hat{W}^{(N,N+2)}, \quad (1)$$

where $\hat{O}^{(N)} = \hat{P}_N^\dagger \hat{O} \hat{P}_N$ and $\hat{O}^{(N,N')} = \hat{P}_N^\dagger \hat{O} \hat{P}_{N'}$, for an operator \hat{O} , with \hat{P}_N , a projection operator onto the $[N]$ boson space. Here $\hat{H}_A^{(N)}$ represents the so-called normal (N boson space) configuration and $\hat{H}_B^{(N+2)}$ represents the so-called intruder ($N+2$ boson space) configuration, which we have assumed, as in [17] where a similar calculation was done for the $_{42}\text{Mo}$ isotopes, to be a proton excitation across the subshell closure at proton number 40 (see Fig. 1 of [17]). The explicit form of these Hamiltonians is

$$\hat{H}_A = \epsilon_d^{(A)} \hat{n}_d + \kappa^{(A)} \hat{Q}_\chi \cdot \hat{Q}_\chi, \quad (2a)$$

$$\hat{H}_B = \epsilon_d^{(B)} \hat{n}_d + \kappa^{(B)} \hat{Q}_\chi \cdot \hat{Q}_\chi + \kappa'^{(B)} \hat{L} \cdot \hat{L} + \Delta_p, \quad (2b)$$

$$\hat{W} = \omega [(d^\dagger \times d^\dagger)^{(0)} + (s^\dagger)^2] + \text{H.c.}, \quad (2c)$$

where the quadrupole operator is defined as $\hat{Q}_\chi = d^\dagger s + s^\dagger \tilde{d} + \chi (d^\dagger \times \tilde{d})^{(2)}$ and \hat{n}_d is the d -boson number operator. In Eq. (2b), Δ_p is the off-set between the normal and intruder configurations, where the index p denotes the fact that this is a proton excitation. The resulting eigenstates $|\Psi; L\rangle$ with angular momentum L , are linear combinations of the wave functions, Ψ_A and Ψ_B , in the two spaces $[N]$ and $[N+2]$,

$$|\Psi; L\rangle = a |\Psi_A; [N], L\rangle + b |\Psi_B; [N+2], L\rangle, \quad (3)$$

with $a^2 + b^2 = 1$.

By employing the IBM-CM framework described above, we have calculated the spectra and other observables of the entire chain of Zr isotopes, from neutron number 52 to 70. The values of the Hamiltonian parameters, obtained by a global fit to energy and $E2$ data, are

*e-mail: noam.gavrielov@mail.huji.ac.il

**e-mail: ami@phys.huji.ac.il

***e-mail: francesco.iachello@yale.edu

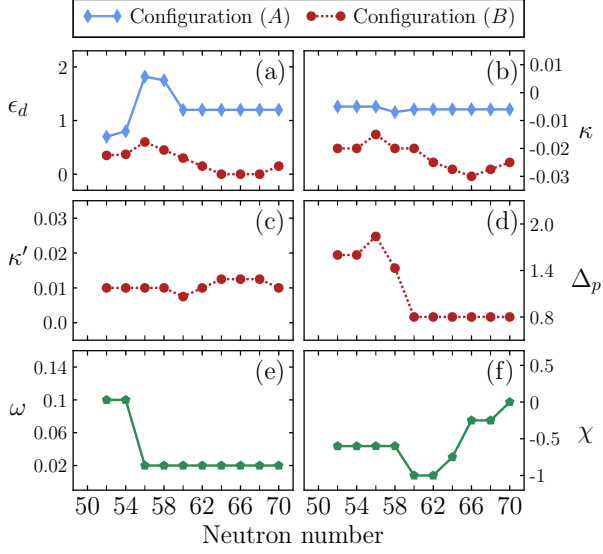


Figure 1. Parameters of the IBM-CM Hamiltonians, Eq. (2) are in MeV and χ is dimensionless. Configurations A and B correspond to boson spaces $[N]$ and $[N+2]$, respectively, with $N=1, 2, \dots, 8$ ($N=7, 6$), for neutron number 52-66 (68,70).

shown in Fig. 1. It should be noted that beyond the middle of the shell, at neutron number 66, bosons are replaced by boson holes [15]. Apart from some fluctuations due to the subshell closure at neutron number 56 (the filling of the $2d_{5/2}$ orbital), the values of the parameters are a smooth function of neutron number and, in some cases, a constant. A notable exception is the sharp decrease by 1 MeV of the energy off-set parameter Δ_p beyond neutron number 56. Such a behavior was observed for the Mo and Ge chains [17, 18] and, as noted in [17], it reflects the effects of the isoscalar residual interaction between protons and neutrons occupying the partner orbitals $1g_{9/2}$ and $1g_{7/2}$, which is the established mechanism for descending cross shell-gap excitations and onset of deformation in this region [19, 20]. The $E2$ operator reads $\hat{T}(E2) = e^{(A)}\hat{Q}_\chi^{(N)} + e^{(B)}\hat{Q}_\chi^{(N+2)}$, where $\hat{Q}_\chi^{(N)} = \hat{P}_N^\dagger \hat{Q}_\chi \hat{P}_N$, $\hat{Q}_\chi^{(N+2)} = \hat{P}_{N+2}^\dagger \hat{Q}_\chi \hat{P}_{N+2}$ and \hat{Q}_χ is the same operator as in the Hamiltonian (2). Here $e^{(A)} = 0.9$ and $e^{(B)} = 2.24$ (W.u.)^{1/2} are the boson effective charges.

In Fig. 2 we show a comparison between experimental and calculated levels. One can see here a rather complex structure. In the region between neutron number 50 and 56, there appear to be two configurations, one spherical (seniority-like), (A), and one weakly deformed, (B), as evidenced by the ratio $R_{4/2}$, which is at 52-56, $R_{4/2}^{(A)} \cong 1.6$ and $R_{4/2}^{(B)} \cong 2.3$. From neutron number 58, there is a pronounced drop in energy for the states of configuration B and at 60, the two configurations exchange their role indicating a Type II QPT. At this stage, the intruder configuration (B) appears to be at the critical point of a U(5)-SU(3) Type I QPT, as evidenced by the low value of the excitation energy of the first excited 0^+ state of this configuration (the 0_3^+ state in ^{100}Zr shown in Fig. 4). The same situation is seen in the ^{62}Sm and ^{64}Gd isotopes at neutron

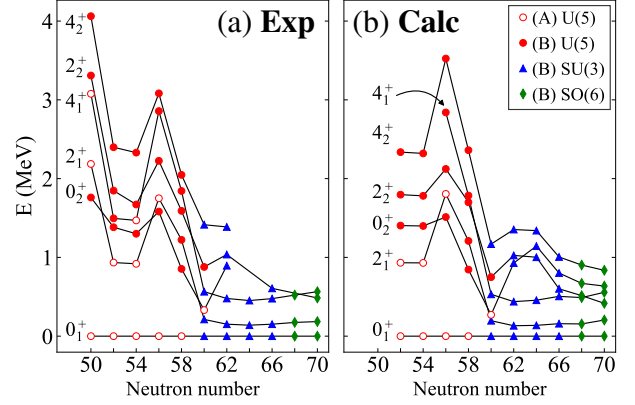


Figure 2. Comparison between (a) experimental [8, 21] and (b) calculated energy levels $0_1^+, 2_1^+, 4_1^+, 0_2^+, 2_2^+, 4_2^+$. Empty (filled) symbols indicate a state dominated by the normal A-configuration (intruder B-configuration), with assignments based on the decomposition of Eq. (3). The shape of the symbol \circ, ∇, \diamond , indicates the closest dynamical symmetry [U(5), SU(3), SO(6)] relevant to the level considered. Note that the calculated values start at neutron number 52, while the experimental values include the closed shell at 50. Adapted from [5].

number 90 [15]. Beyond neutron number 60, the intruder configuration (B) is strongly deformed, as evidenced by the small value of the excitation energy of the state 2_1^+ , $E_{2_1^+} = 139.3$ keV and by the ratio $R_{4/2}^{(B)} = 3.24$ in ^{104}Zr . At still larger neutron number 66, the ground state band becomes γ -unstable as evidenced by the close energy of the states 2_2^+ and 4_1^+ , $E_{2_2^+} = 607.0$ keV, $E_{4_1^+} = 476.5$ keV, in ^{106}Zr , and especially by the recent results $E_{4_1^+} = 565$ keV and $E_{2_2^+} = 485$ keV in ^{110}Zr [8], a signature of the SO(6) symmetry. In this region, the ground state configuration undergoes a crossover from SU(3) to SO(6).

The above spectral analysis signals the presence of co-existing Type I and Type II QPTs, which is the defining property of IQPTs. In order to understand the nature of these phase transitions, one needs to study the behavior of the order parameters. The latter are given by

$$\frac{\langle \hat{n}_d \rangle_A}{\langle \hat{N} \rangle_A}, \quad \frac{\langle \hat{n}_d \rangle_B}{\langle \hat{N} \rangle_B}, \quad \frac{\langle \hat{n}_d \rangle_{0_1^+}}{\langle \hat{N} \rangle_{0_1^+}}. \quad (4)$$

They involve the expectation value of \hat{n}_d in the ground state wave function, $|\Psi; L=0_1^+\rangle$ and in its Ψ_A and Ψ_B components (3), normalized by the respective boson numbers, $\langle \hat{N} \rangle_A = N$, $\langle \hat{N} \rangle_B = N+2$, $\langle \hat{N} \rangle_{0_1^+} = a^2 N + b^2 (N+2)$. Here $\langle \hat{n}_d \rangle_A$ and $\langle \hat{n}_d \rangle_B$ portray the shape-evolution in configuration (A) and (B), respectively, and $\langle \hat{n}_d \rangle_{0_1^+} = a^2 \langle \hat{n}_d \rangle_A + b^2 \langle \hat{n}_d \rangle_B$ contains information on the normal-intruder mixing. Fig. 3(a) shows the evolution of the order parameters involving $\langle \hat{n}_d \rangle_A$ and $\langle \hat{n}_d \rangle_B$ in dotted lines, and $\langle \hat{n}_d \rangle_{0_1^+}$ in solid line. Configuration (A) is seen to be spherical for all neutron numbers considered. In contrast, configuration (B) is weakly-deformed for neutron number 52-58. One can see here clearly a jump between neutron number 58 and 60 from configuration (A) to configuration (B), indicating a 1st order Type II phase transition [3], a further increase

at neutron numbers 60-64 indicating a U(5)-SU(3) Type I QPT, and, finally, there is a decrease at neutron number 66, due in part to the crossover from SU(3) to SO(6) and in part to the shift from boson particles to boson holes after the middle of the major shell 50-82. $\langle \hat{n}_d \rangle_{0_1^+}$ is close to $\langle \hat{n}_d \rangle_A$ for neutron number 52-58 and coincides with $\langle \hat{n}_d \rangle_B$ above 60, indicating a high degree of purity and small configuration-mixing, with the exception of a narrow transition region. Indeed, the ground state wave function (3) has $a^2 = 98.2\%$, $b^2 = 87.2\%$ and $b^2 = 99.9\%$ for ^{98}Zr , ^{100}Zr and ^{102}Zr , respectively. These conclusions are stressed by an analysis of other observables, in particular, the $B(E2)$ values. As shown in Fig. 3(b), the calculated $B(E2)$'s agree with the empirical values and follow the same trends as the respective order parameters.

Further evidence can be obtained from an analysis of the isotope shift $\Delta \langle \hat{r}^2 \rangle_{0_1^+} = \langle \hat{r}^2 \rangle_{0_1^+; A+2} - \langle \hat{r}^2 \rangle_{0_1^+; A}$, where $\langle \hat{r}^2 \rangle_{0_1^+}$ is the expectation value of \hat{r}^2 in the ground state 0_1^+ . In the IBM-CM the latter is given by $\langle \hat{r}^2 \rangle = r_c^2 + \alpha N_v + \eta [\langle \hat{n}_d^{(N)} \rangle + \langle \hat{n}_d^{(N+2)} \rangle]$, where r_c^2 is the square radius of the closed shell, N_v is half the number of valence particles, and η is a coefficient that takes into account the effect of deformation [15, 24]. $\Delta \langle \hat{r}^2 \rangle_{0_1^+}$ depends on two parameters, $\alpha = 0.235$, $\eta = 0.264 \text{ fm}^2$, whose values are fixed by the procedure of Ref [24]. $\Delta \langle \hat{r}^2 \rangle_{0_1^+}$ should increase at the transition point and decrease and, as seen in Fig. 3(c), it does so, although the error bars are large and no data are available beyond neutron number 60. Similarly, the two-neutron separation energies S_{2n} can be written as [15], $S_{2n} = -\tilde{A} - \tilde{B}N_v \pm S_{2n}^{\text{def}} - \Delta_n$, where S_{2n}^{def} is the contribution of the deformation, obtained by the expectation value of the Hamiltonian in the ground state 0_1^+ . The + sign applies to particles and the - sign to holes, and Δ_n takes into account the neutron subshell closure at 56, $\Delta_n = 0$ for 50-56 and $\Delta_n = 2 \text{ MeV}$ for 58-70. The value of Δ_n is taken from Table XII of [25] and $\tilde{A} = -16.5$, $\tilde{B} = 0.758 \text{ MeV}$ are determined by a fit to binding energies of $^{92,94,96}\text{Zr}$. The calculated S_{2n} , shown in Fig. 3(d), displays a complex behavior. Between neutron number 52 and 56 it is a straight line, as the ground state is spherical (seniority-like) configuration (A). After 56, it first goes down due to the subshell closure at 56, then it flattens as expected from a 1st order Type I QPT (see, for example the same situation in the ^{62}Sm isotopes [15]). After 62, it goes down again due to the increasing of deformation and finally it flattens as expected from a crossover from SU(3) to SO(6).

We note that our calculations describe the experimental data in the entire range $^{92-110}\text{Zr}$ very well. Here we show only two examples, ^{100}Zr and ^{110}Zr . ^{100}Zr is near the critical point of both Type I and Type II QPT and yet our description of energy levels and $B(E2)$ values is excellent, Fig. 4(a)-(b). The ground state band, configuration (B), appears to have features of the so-called X(5) symmetry [26], while the spherical configuration (A) has now become the excited band 0_2^+ . ^{110}Zr , Fig. 4(c)-(d), appears instead to be an excellent example of SO(6) symmetry [15], although few experimental data are available. In general, the current results resemble those obtained in the MCSM [14], however, there are some noticeable differences. Specifically,

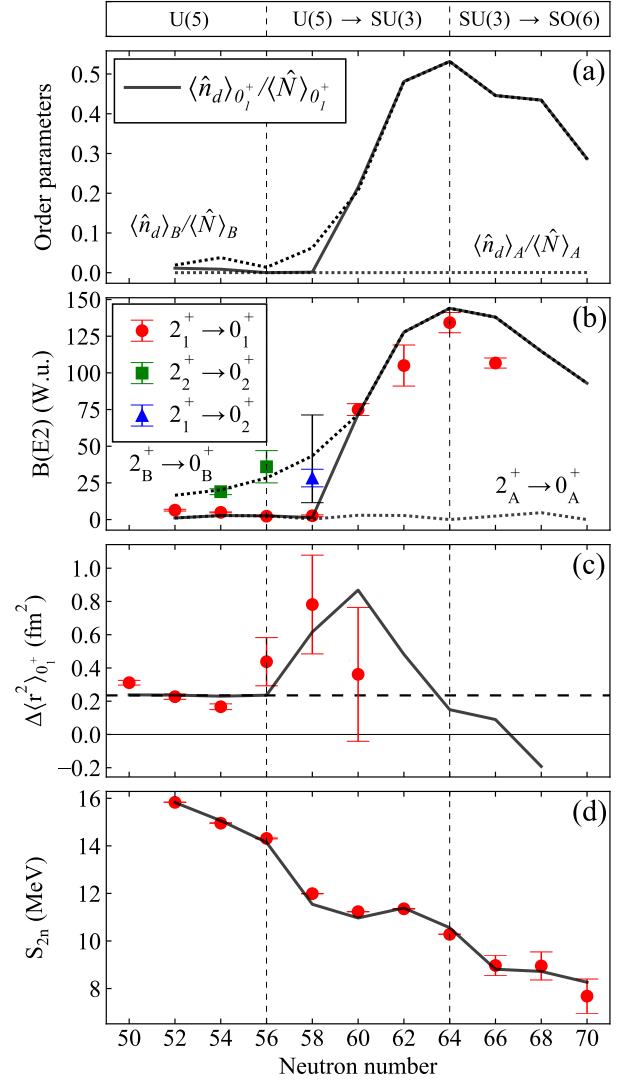


Figure 3. Evolution of order parameters and of observables along the Zr chain. Symbols (solid lines) denote experimental data (calculated results). (a) Order parameters, Eq. (4). Notation of lines is explained in the text. (b) $B(E2)$ values in Weisskopf units (W.u.). Data taken from [6, 7, 9, 10, 21]. Dotted lines denote calculated $E2$ transitions within a configuration. (c) Isotope shift, $\Delta \langle \hat{r}^2 \rangle_{0_1^+}$ in fm^2 . Data taken from [22]. The horizontal dashed line at 0.235 fm^2 represents the smooth behavior in $\Delta \langle \hat{r}^2 \rangle_{0_1^+}$ due to the $A^{1/3}$ increase of the nuclear radius. (d) Two-neutron separation energies, S_{2n} , in MeV. Data taken from AME2016 [23]. Adapted from [5].

the replacement γ -unstable \rightarrow triaxial and the inclusion of more than two configurations in the MCSM. The spherical state in ^{100}Zr is identified in the MCSM as 0_4^+ , in contrast to 0_2^+ in the current calculation and the data. Both calculations show a large jump in $B(E2; 2_1^+ \rightarrow 0_1^+)$, between ^{98}Zr and ^{100}Zr , typical of a 1st order QPT. This is in contrast with mean-field based calculations [11–13], which due to their character smooth out the phase transitional behavior, and show no such jump at the critical point of the QPT (see Fig. 2 of [10]). The observed peak in $B(E2; 2_1^+ \rightarrow 0_1^+)$ for ^{104}Zr , is reproduced here but not by the MCSM.

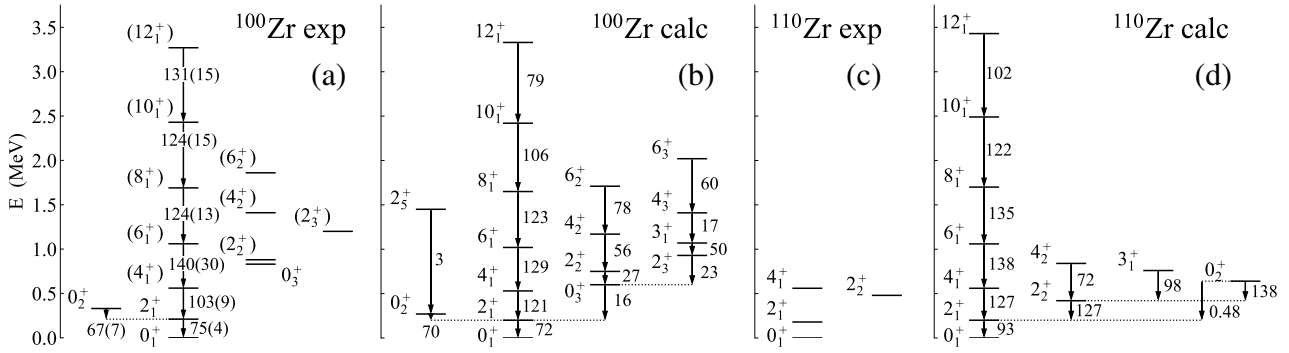


Figure 4. Experimental and calculated energy levels in MeV and $E2$ rates in W.u. for ^{100}Zr and ^{110}Zr . Adapted from [5].

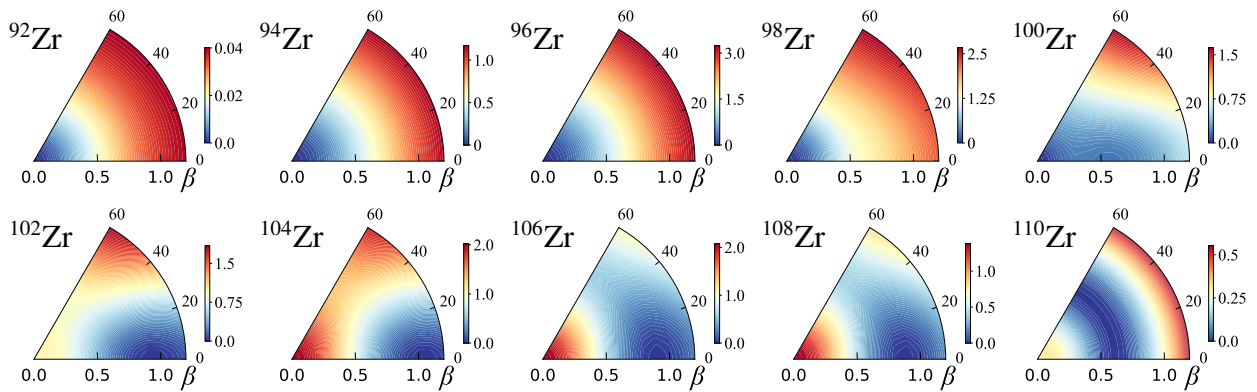


Figure 5. Contour plots in the (β, γ) plane of the classical potential surface for the $^{92-110}\text{Zr}$ isotopes. Adapted from [5].

The algebraic approach allows both a quantum and a classical analysis of QPTs. Classical potential surfaces are obtained by the method of matrix-coherent-states [3]. As seen in Fig. 5, the calculated surfaces confirm the quantum results, as they show a transition from spherical ($^{92-98}\text{Zr}$), to a flat-bottomed potential at ^{100}Zr , to axially deformed ($^{102-104}\text{Zr}$), and finally to γ -unstable ($^{106-110}\text{Zr}$).

This work was supported in part by U.S. DOE under Grant No. DE-FG02-91ER-40608 and by the US-Israel Bination Science Foundation Grant No. 2016032.

References

- [1] P. Cejnar, J. Jolie and R. F. Casten, *Rev. Mod. Phys.* **82**, 2155 (2010).
- [2] K. Heyde and J. L. Wood, *Rev. Mod. Phys.* **83**, 1467 (2011).
- [3] A. Frank, P. Van Isacker and F. Iachello, *Phys. Rev. C* **73**, 061302(R) (2006).
- [4] J. E. García-Ramos and K. Heyde, *Phys. Rev. C* **89**, 014306 (2014); *Phys. Rev. C* **92**, 034309 (2015).
- [5] N. Gavrielov, A. Leviatan and F. Iachello, *Phys. Rev. C* **99**, 064324 (2019).
- [6] C. Kremer *et al.*, *Phys. Rev. Lett.* **117**, 172503 (2016).
- [7] S. Ansari *et al.*, *Phys. Rev. C* **96**, 054323 (2017).
- [8] N. Paul *et al.*, *Phys. Rev. Lett.* **118**, 032501 (2017).
- [9] W. Witt *et al.*, *Phys. Rev. C* **98**, 041302(R) (2018).
- [10] P. Singh *et al.*, *Phys. Rev. Lett.* **121**, 192501 (2018).
- [11] J.-P. Delaroche *et al.*, *Phys. Rev. C* **81**, 014303 (2010).
- [12] H. Mei *et al.*, *Phys. Rev. C* **85**, 034321 (2012).
- [13] K. Nomura *et al.*, *Phys. Rev. C* **94**, 044314 (2016).
- [14] T. Togashi, Y. Tsunoda, T. Otsuka and N. Shimizu, *Phys. Rev. Lett.* **117**, 172502 (2016).
- [15] F. Iachello and A. Arima, *The Interacting Boson Model*, (Cambridge Univ. Press, Cambridge, 1987).
- [16] P. D. Duval and B. R. Barrett, *Phys. Lett. B* **100**, 223 (1981); *Nucl. Phys. A* **376**, 213 (1982).
- [17] M. Sambataro and G. Molnár, *Nucl. Phys. A* **376**, 201 (1982).
- [18] P. D. Duval *et al.*, *Phys. Lett. B* **124**, 297 (1983).
- [19] P. Federman and S. Pittel, *Phys. Rev. C* **20**, 820 (1979).
- [20] K. Heyde *et al.*, *Phys. Lett. B* **155**, 303 (1985).
- [21] Evaluated Nuclear Structure Data File (ENSDF), <https://www.nndc.bnl.gov/ensdf/>.
- [22] I. Angeli and K. P. Marinova, *At. Data Nucl. Data Tables* **99**, 69 (2013).
- [23] M. Wang *et al.*, *Chinese Phys. C* **41**, 030003 (2017).
- [24] S. Zerguine *et al.*, *Phys. Rev. C* **85**, 034331 (2012).
- [25] J. Barea and F. Iachello, *Phys. Rev. C* **79**, 044301 (2009).
- [26] F. Iachello, *Phys. Rev. Lett.* **87**, 052502 (2001).

